LAWRENCE
LIVERMORE
NATIONAL
LABORATORY

LLNL-TR-615452

Real-Time Vehicle-Mounted Multistatic Ground Penetrating Radar Imaging System for Buried Object Detection

D. H. Chambers, D. W. Paglieroni, J. E. Mast, N. R. Beer

February 4, 2013

Disclaimer

This work performed under the auspices of the U.S. Department of Energy by Lawrence Livermore National Laboratory under Contract DE-AC52-07NA27344.

Real-Time Vehicle-Mounted Multistatic Ground Penetrating Radar Imaging System for Buried Object Detection

David H. Chambers, David W. Paglieroni, Jeffrey E. Mast, N. Reginald Beer
June 29, 2011

1 Abstract

A multistatic ground penetrating radar system is described, capable of real-time imaging and object detection. The radar consists of 16 transmitter and receiver pairs mounted across the front of a vehicle. The transmitters operate sequentially with all receivers activated for each transmit pulse. The resulting frame of 256 multistatic time signals is processed into an image using a tomographic reconstruction technique. In this paper we describe the system architecture, signal conditioning, and reconstruction algorithm for producing a sequence of images in real time as the vehicle travels across the ground. We demonstrate a robust image post-processing method that separates the bright spot corresponding to the dominant buried object in an image frame from the background. This is essential before calculating an energy-based statistic for automatic detection of buried objects. This spot ratio detection statistic, based on energy both inside and outside the spot, is shown to be not only more stationary than spot energy (i.e. mostly free of localized trends due to changing ground conditions), but also more powerful as a detection statistic. Finally, we demonstrate that multistatic imaging significantly improves the detection performance over more conventional monostatic array processing.

2 Introduction

Ground Penetrating Radar (GPR) systems are widely used for detecting buried objects such as landmines and utility pipes. Unlike metal detectors that use electromagnetic induction (EMI) loops, GPRs can detect not only buried metallic objects, but also buried non-metallic objects of sufficient dielectric contrast against soil. High frequency GPR systems that detect shallow buried objects such as landmines range from handheld single antenna systems, to multiple antenna arrays mounted on ground or aerial platforms [14, 15]. Vehicle mounted systems are particularly useful for rapidly surveying wide areas. In nearly all vehicle-mounted systems the transmitter and receiver arrays are designed to operate monostatically (or more precisely, multi-monostatically) [14], *i.e.* the transmitters and receivers are approximately co-located to form a sequence of monostatic pairs. When a given transmitter emits a pulse, only the corresponding receiver is activated. The monostatic pairs operate sequentially to create one *frame* of radar return signals each time the system completes one full cycle of transmitter activations. Each radar return signal measures backscattered energy from the ground and buried objects along the direction of a specific transmitter-receiver pair. In this sense, a frame of radar return signals measures backscattered energy from an object over a range of different look directions.

The signals from monostatic real-time GPR systems are usually analyzed directly for evidence of buried object [45, 44, 10, 53, 47]. The signals are typically organized into signal scans, i.e., sequences of radar return signals acquired by specific transmitter-receiver pairs as the vehicle moves down-track. The input is one signal scan for each of N monostatic transmitter-receiver pairs. Buried objects present hyperbolic arc-like signatures in signal scans due to the systematic change in range as the array approaches and recedes from a buried object. It is common practice to first detect anomalies in the return signals [45] and then apply more sophisticated algorithms that (1) determine if the anomalies are hyperbolic in nature [36, 53, 42], or (2) use trained classifiers to distinguish buried objects of interest from false positives [43, 50, 38, 3, 4, 21, 28, 51, 22, 52, 19, 20, 18, 47, 40].

GPR arrays can also operate in multistatic mode. In this case, all receivers are activated when a transmitter emits a pulse. For each transmitted pulse, measurements of the scattered energy are obtained at multiple angles from the transmitter look direction. One frame from a multistatic array of N transmitter-receiver pairs contains N^2 radar return signals, compared with the N signals in a frame from a monostatic array with the same number of elements. Thus, multistatic GPR arrays collect much more information about the ground and subsurface in a single frame than monostatic arrays. However, this comes at the cost of greater system complexity and data processing requirements to extract useful information.

In this paper we describe a novel field-tested multistatic GPR array system, the Multistatic Underground Imaging Radar (MUIR), capable of real-time imaging and object detection. Our approach is to reconstruct a sequence of GPR tomography images in real-time from the sequence of GPR signal frames acquired as the vehicle moves down-track, and then extract buried object detection statistics from those images. Each multistatic data frame of N^2 signals is reduced to a single image in a vertical plane perpendicular to the vehicle track (cross-track direction). Successive image frames can be subsequently combined using a synthetic aperture approach to provide focusing in the down-track direction. The effect is to reduce both the cross-track and down-track hyperbolas associated with buried objects to bright spots in an image sequence. Bright spot detection is arguably easier than hyperbola detection, especially when the contrast against background is higher for bright spots than for hyperbolas. However, real-time multistatic GPR imaging does pose a computational challenge. Our MUIR system addresses this challenge by hosting fast imaging algorithms on a vehicle-mounted computer cluster.

Multistatic array operation is common in tomographic imaging [26]. Indeed, most of the previous work in multistatic GPR is motivated by the problem of tomographic imaging or inversion ([24, 39, 2], among others) and typically involves theoretical studies using simulated data. Small systems have more recently been developed for investigating multistatic GPR in the laboratory [54, 11, 1, 9, 5]. Many of these systems were motivated by the success of time-reversal processing techniques for multistatic array data [12, 13, 46, 35, 34, 16, 17]. The authors are aware of only two examples of multistatic GPR systems tested in field conditions: a side-looking multistatic SAR system [31, 32] and a forward looking vehicle-mounted SAR system [27]. The system in [31, 32] contains one transmitter and one receiver whose separations are manually adjusted between scans to obtain multiple images from different configurations. The system in [27] uses a single transmit horn and single receive horn mounted on mechanical

translation stages that move independently. Both systems employ wideband stepped frequency radars and were used primarily for research purposes. Neither was designed for rapid real-time operation.

Though multistatic GPR arrays have in principle many potential advantages over multi-monostatic arrays, the main technical challenges are the additional system complexity and the computational cost of processing the frames of radar return signals in real-time. In this article we show how these challenges are met in our MUIR system, providing a capability of real-time multistatic imaging and object detection. In section 3 we provide a general description of the MUIR system and its general capabilities. In sections 4-7 we describe the major processing steps, namely GPR signal pre-processing, imaging, image post-processing, and calculation of a detection statistic for buried objects. Finally in section 8 we show performance results obtained from a recent trial at a test facility in the western United States. The overall conclusion is that multistatic GPR arrays are now a practical reality and show good object detection performance. However, we are only beginning to exploit the information potential of multistatic GPR data. We expect to see dramatic improvements in detection and classification performance as more sophisticated algorithms specifically designed for multistatic GPR data are developed and incorporated into our real-time processing system.

3 System Description

Our impulse radar array contains $N = 16$ transmitters and $N = 16$ receivers. It uses 32 "folded-hex" time domain horn antennas on two tracks of length 2 meters separated by roughly 10 cm and mounted to the front of a vehicle (Fig 1). The array is mounted on a mechanically adjustable pivot that allows the radar look direction to be adjusted from vertical (pointing straight into the ground) to an angle of 60° from vertical. In the tilt forward configuration, the imaging plane is a vertical plane in front of the array at the distance where the array boresight intersects the ground plane. The array *boresight* is defined as the line beginning midway between transmitter and receiver lines (pivot axis) and pointing in the direction of the antennas (Fig. 2). For our transmitters, the beam width as measured from the boresight axis to the 3dB point is $\approx 50^\circ$. The coordinate axes are defined as $+x$ in the cross-track direction along the array (from the driver to the passenger side of the vehicle), $+y$ in the down-track direction, and $+z$ vertically upward.

The array system fires a 4 ns pulse from each transmitter in sequence, collecting return signals on each of the $N = 16$ receivers for each transmit pulse. Each received signal is 512 samples long with a 40 ps time interval between samples. Each signal thus has a duration of approximately 20 ns. The entire data frame of $N^2 = 256$ received signals is acquired in 4 ms. In addition to the GPR array, the system includes several GPS receivers for geolocating buried objects, a temperature sensor, and other sensors for system diagnostics, tracking, and control.

As the vehicle moves down-track, a real-time processing system creates a vertical plane image in the cross-track direction (an image frame) and calculates a detection statistic for each such frame. The four processing steps are (i) GPR signal preprocessing, (ii) GPR imaging, (iii) GPR image post-processing, and (iv) buried object detection. These processing steps along with data acquisitions are divided between two processors: a Storage and Track Processing (STP) unit and a Real Time/Visualization (RTV) unit. The STP unit handles data acquisition and GPR signal

preprocessing, control, and system monitoring. It also combines the GPS and other navigational data with the GPR data to allow precise geospatial location of buried objects. It consists of 24 thread execution engines (dual hex core hyperthreaded processors) with 24 GB of RAM, a 256 GB SSD OS disk, and dual 1.5 TB RAID 6 storage for archiving raw data. It passes the preprocessed signals to the RTV unit for imaging, image post-processing, buried object detection, and visualization. The RTV unit has a dual hex core CPU and NVIDIA Tesla GPU with two 256 GB SSD hard drives. Both units have an IPMI interface, 4 Gb network ports for communication, and are DC powered. The processing system is ruggedized for off-track real-time operation. Figure 3 shows a diagram of the computational system and communication requirements. The system has been tested at a desert facility in the southwestern United States and on a local test track at Lawrence Livermore National Laboratory.

Figure 1: Photo of 32 element multistatic array alone (top) and mounted on vehicle (bottom) in field configuration.

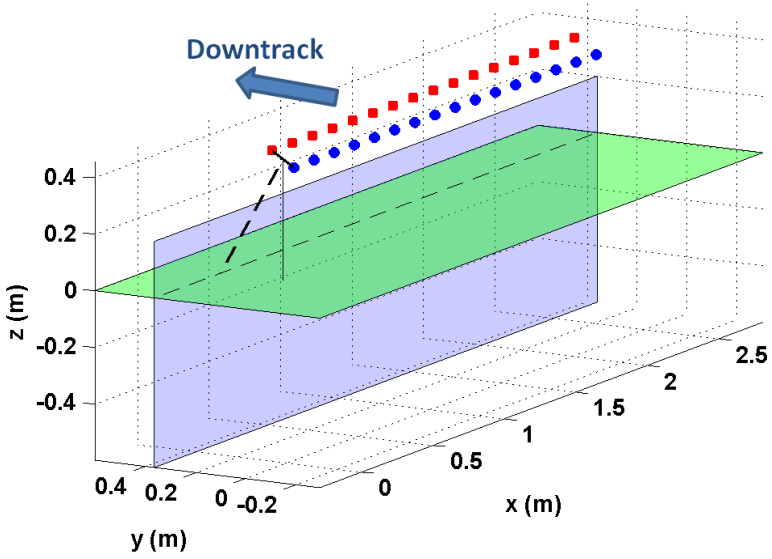

Figure 2: Array and imaging geometry for nominal height of 40 cm and forward look direction of 30°. Transmitters (red squares) and receivers (blue circles) are separated by 10 cm. The vertical image plane (purple) intersects the ground plane (green) at a position in front of the array defined by the projection of the array axis in the boresight direction(30°).

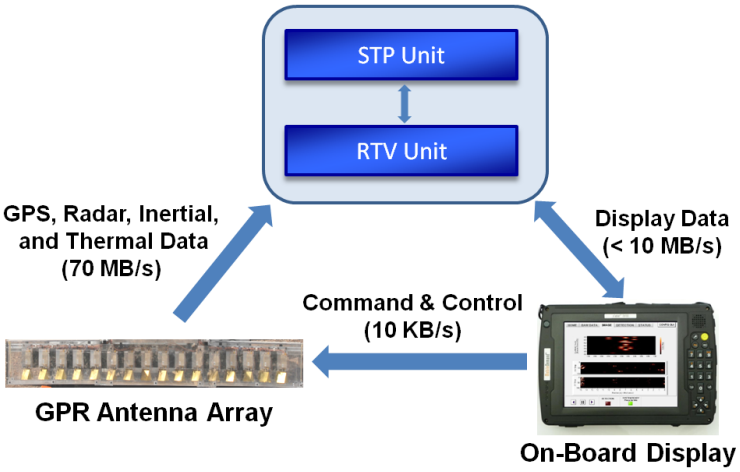

Figure 3: Block diagram of our real-time multistatic GPR imaging and processing system for buried object detection.

4 GPR Return Signal Preprocessing

In GPR antenna arrays that are mounted to a moving vehicle a prescribed distance above ground level, the return signals will typically be contaminated by undesired artifacts attributed to external interference, antenna coupling, ground bounce / multipath, and

roughness in the surface. These background artifacts are unrelated to buried objects of interest and can make them much more difficult to detect. The goal of pre-processing is to remove or suppress background in GPR return signals so that buried objects will be easier to detect in the reconstructed tomography images.

Fig. 4(a) shows a down-track scan of GPR return signals associated with a specific transmitter-receiver (TR) pair. A down-track scan is a sequence of GPR return signals for a specific TR pair as the vehicle moves down-track. The horizontal stripes near the top are due to antenna coupling, *i.e.* transmission directly between transmitter and receiver elements in the array. The varying bright stripe below the antenna coupling is due to ground bounce (reflection off an uneven surface). Echos of the surface due to multipath can be seen below the surface reflection. The hyperbola is produced by backscatter from a buried object. The signal associated with a single column in the scan from Fig. 4(a) is shown in Fig. 4(b), along with its spectrum in Fig. 4(c). A signal contaminated by interference is shown in Fig. 4(d). Note that for our system, most of the return energy lies in the range 1-3 GHz. A longer scan is shown in Fig. 5(a).

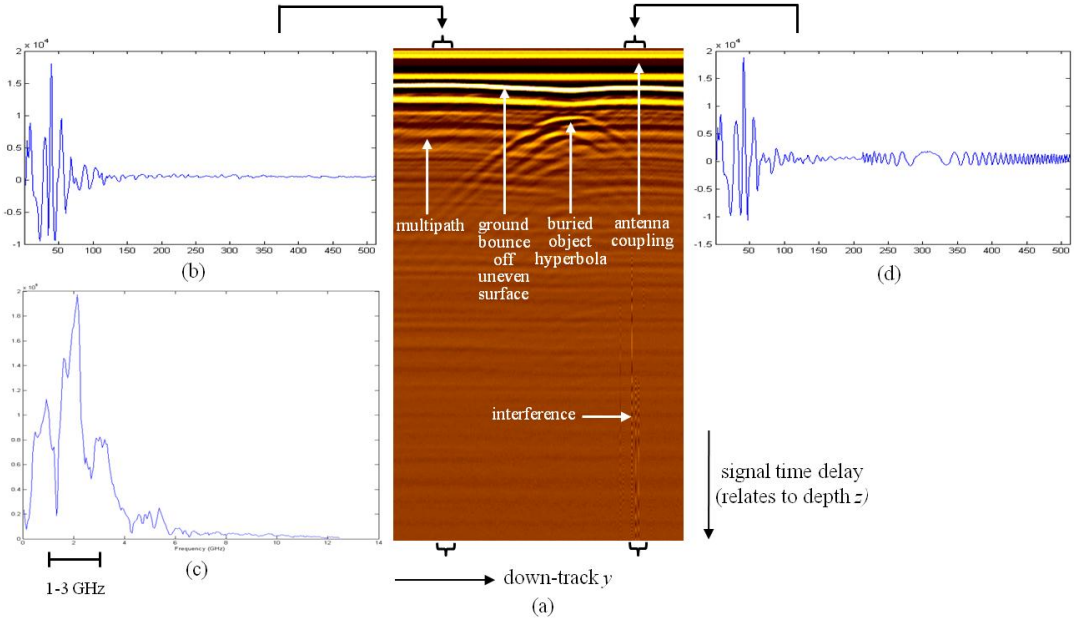

Figure 4: (a) Down-track scan of GPR return signals. (b) Signal with no interference. (c) Amplitude spectrum of signal in (b). (d) Signal contaminated by interference.

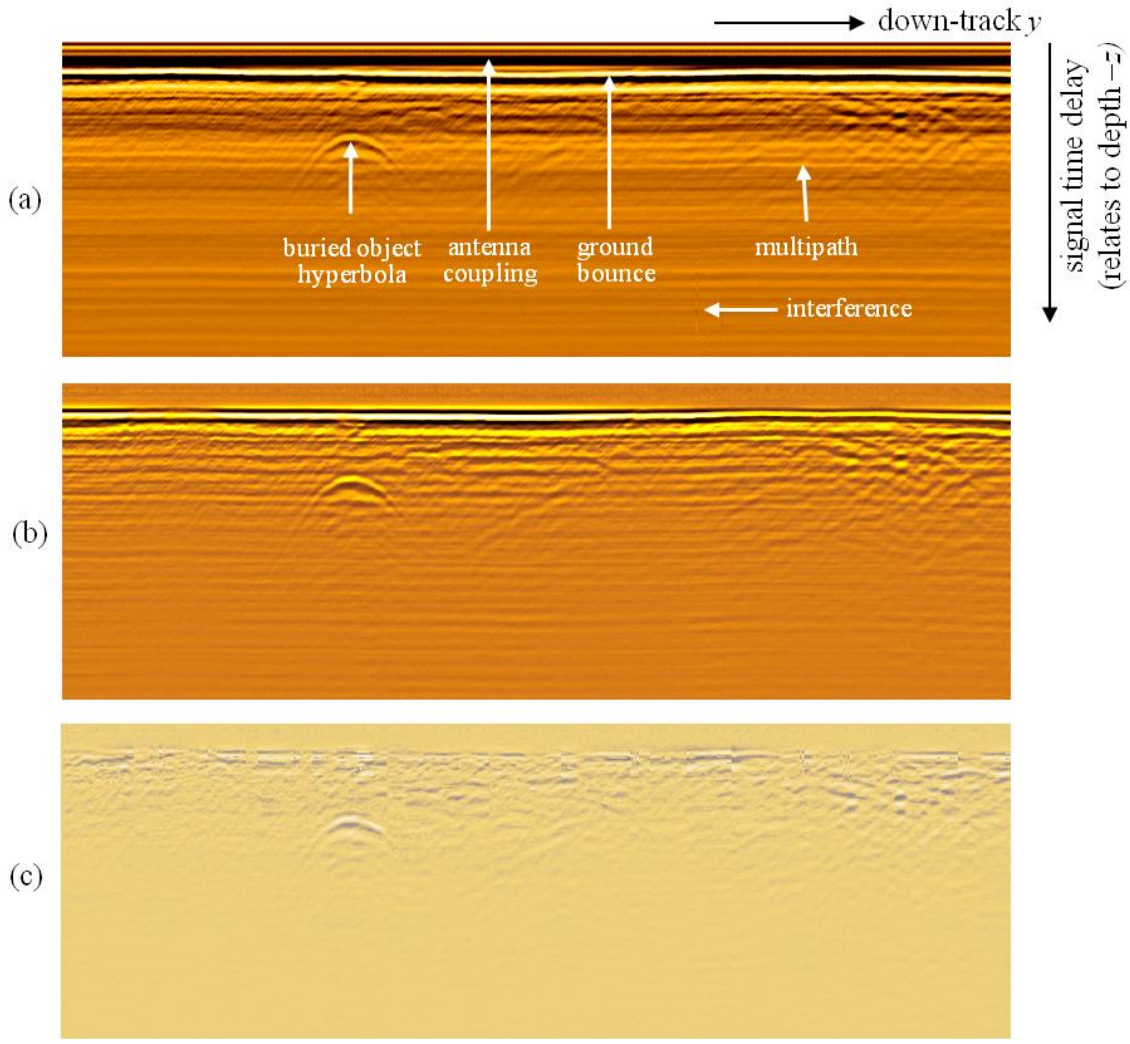

Figure 5: Down-track scans of GPR return signals. (a) Unprocessed. (b) With interference and antenna coupling pulse removed. (c) With ground bounce and multipath suppressed.

Signal pre-processing for background removal usually involves background subtraction. The mean of previous return signals (a background estimate) is normally subtracted from the current signal [7]. The current signal is sometimes first adjusted for scale and shift relative to the mean signal [43, 6, 49]. However, other methods have been considered. For example, background removal was based on LMS in [45, 44], principal components in [10], Kalman filters in [8], and particle filters in [41]. Our approach is to perform background subtraction twice: first to remove antenna coupling, and then to suppress ground bounce / multipath. As discussed below, we perform a second subtraction because along rough roads, the separation between multipath artifacts in a GPR return signal varies with the air gap between the antenna and the surface of the ground.

4.1 Interference Rejection

Signals from external sources operating in the vicinity of the GPR can additively interfere with return signals. As shown in Fig. 5(a), interference disrupts isolated columns of scan data. The usual culprits are GPS communication links, cell phones, and other locally operating communication systems. It is common practice to reject highly transient interference by applying a short duration median filter in the down-track direction to each sample on each row of the scan [36, 44, 6]. The median filters must be short so as to not also destroy hyperbolas associated with buried objects of interest. Although we are developing new methods for rejecting interference of any duration without destroying evidence of buried objects, we currently suppress transient interference by applying median filters that span only three adjacent columns in a scan.

4.2 Coupling Pulse Removal

The coupling pulse between transmit and receive antennas is the return signal component due to the direct path of the transmitted signal to the receiver. Coupling pulses produce horizontal streaks in down-track scans, as they tend to be constant at predictable times associated with first and higher order reflections of transmitted signals off of antenna horns.

One can reduce antenna coupling by (a) using low radar cross-section (RCS) antennas, (b) packing the antennas in radar absorbing material (RAM), or (c) subtracting a predicted return signal from each return signal. For a given TR pair, we form a predicted signal as a weighted mean $\bar{\mathbf{r}}_k$ of return signals prior to the current return signal $\mathbf{r}_k$: $\bar{\mathbf{r}}_k = (1-\alpha)\bar{\mathbf{r}}_{k-1} + \alpha\mathbf{r}_k$ with $\alpha = 0.05$ and $\bar{\mathbf{r}}_0 = \mathbf{r}_0$. Fig. 5(b) shows an example of interference rejection and coupling pulse removal.

4.3 Ground Bounce and Multi-Path Removal

Ground bounce is the portion of the return signal that reflects (bounces) off the surface of the ground. Ground bounce produces a bright curve in the down-track scan that tracks the shape of the surface. In GPR antenna arrays with high RCS, there will also be multiple reflections. *Multipath* is the portion of the return signal due to multiple reflections in the air gap between the array and the ground surface. The effect of multipath on down-track scans is to replicate faint versions of the surface track in the sub-surface (see Fig. 5(a)).

Once interference and antenna coupling have been removed, surface tracking is used to determine the air gap between the antenna array and the surface, and the extent of the air gap is used to suppress ground bounce and multipath. The air gap varies from zero to $1.5h$, where h is nominal height of the antenna array above ground level. In the absence of a buried object, the largest positive peak in the signal (with interference and antenna coupling removed) occurs at the surface. Various constraints are applied to ensure that the surface is properly tracked. Within a scan, the surface is tracked within a time interval Δ_t (a vertical range in Fig. 5(b)) equal to one cycle of the center frequency of the radar. The start of the interval is the point at which the signal amplitude significantly exceeds the noise level. The surface location for a given column in the scan is chosen as the closest peak in signal value within Δ_t of the surface

location for the previous column.

For fixed soil permittivity, the separation between multipath artifacts in a GPR return signal varies with the air gap. Conversely, the separation between multipath artifacts will be constant for all signals associated with a specific air gap. For a specific TR pair, consider the sequence of return signals $\{\mathbf{r}_k\}$ associated with a specific air gap (these are columns of a down-track signal scan that all share the same air gap within a tolerance of a fraction of 1 cm). Assume that interference and antenna coupling have been removed from $\mathbf{r}_k$. $\mathbf{r}_k$ can be modeled as

$$\mathbf{r}_k = \mathbf{s}_k + \mathbf{b}_k \tag{1}$$

where $\mathbf{s}_k$ free of ground bounce and multipath, and $\mathbf{b}_k$ is the background component that takes everything other than buried objects into account. We estimate $\mathbf{s}_k$ as

$$\mathbf{s}_k \approx \mathbf{r}_k - \hat{\mathbf{b}}_k \tag{2}$$

$$\hat{\mathbf{b}}_k = \begin{cases} \mathbf{r}_0 & k = 0 \\ (1-\alpha)\hat{\mathbf{b}}_{k-1} + \alpha\mathbf{r}_{k-1} & k > 0 \end{cases} \quad (\alpha = 0.05) \tag{3}$$

We are currently investigating ways of extending this approach to minimize the effect of anomalous return signals on the background estimate. Fig. 5(c) shows an example of ground bounce and multipath suppression for the down-track scan associated with a particular TR pair (as each such pair is processed separately).

4.4 Surface Flattening

Surface roughness tends to increase the buried object false positive rate. When the surface is rough, anomalies in radar returns caused by unusually high levels of backscatter from the surface become much more probable. Ground bounce removal might mitigate this effect to some degree. Surface roughness also makes image background estimation more difficult by contributing to air pockets in reconstructed GPR images. We address this problem by flattening the surface prior to GPR image reconstruction. Flattening is accomplished by shifting the columns in the down-track scan for each TR pair such that for every column, the first row of the scan always lies at the surface.

5 GPR Image Reconstruction

After preprocessing, each acquired data frame contains a set of time traces or GPR return signals $\{R_{mn}(t) : m = 1,\ldots,16; n = 1,\ldots,16\}$, where $R_{mn}(t)$ is the time trace from receiver *n* obtained when the transmitter *m* emitted a pulse, and our array contains $N = 16$ transmitter-receiver pairs. Each data frame thus contains $N^2 = 256$ time traces. A *real aperture radar (RAR)* image frame is reconstructed in the *xz* plane (a vertical plane in the cross-track direction). The radar return signals for each RAR image frame are received through a *real aperture* (the array of receiver antennas that travels with the vehicle). As mentioned in section 3, one fully multistatic frame of N^2 signals is acquired every 4 ms, during which the array travels less than 1 cm at typical operation speeds (≈ 8 km/hr). By tilting the array forward, the ground reflection and associated multi-path is reduced, and objects can be

detected ahead of the array position. In particular, if the antenna array is at location y_j down-track, then the image plane occurs at $y_j^I = y_j + h\tan(\phi)$, where h is antenna height above the ground plane, and ϕ is the forward tilt of the antenna array from vertical. The array pivots around an axis midway between sequences of transmitters and receivers. When the array is tilted forward, transmitter height decreases and receiver height increases from the nominal array height. The separation between transmitter and receiver in the downtrack (*y*) direction is also reduced. The vertical xz image plane contains the intersection of the horizontal ground plane and the tilted plane that contains the boresight axes of the transmitters (Fig. 2). It approximates the region of maximum overlap between the beam patterns of the transmitter and receiver antennas in the ground (Fig. 6). These patterns are oriented closer to the vertical in the ground due to refraction at the ground-air interface.

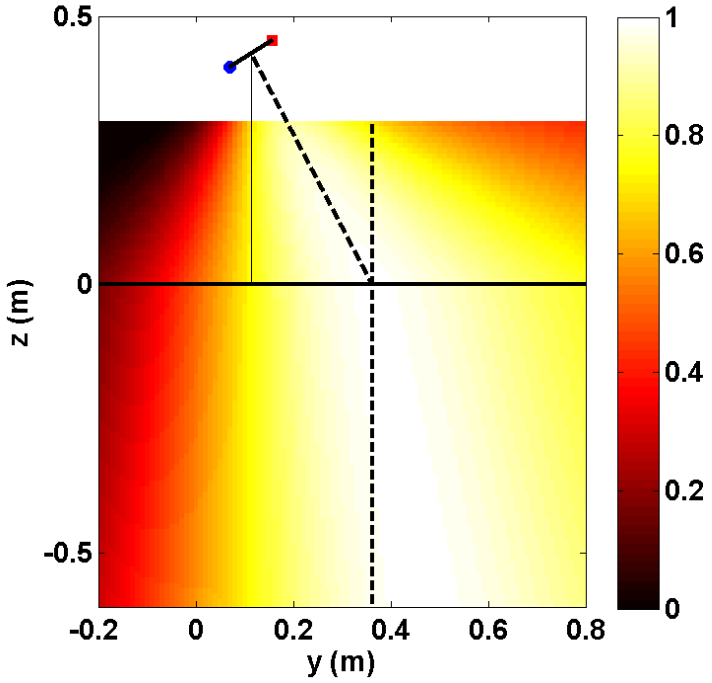

Figure 6: Imaging geometry and beam patterns for an array of nominal height of 40 cm and look direction of 30°. Shown are the positions of the ground (solid line) and image plane (vertical dashed line) superposed on the product of the transmitter and receiver beam patterns ($\cos\theta$ for each) for soil with refractive index of three.

Our imaging algorithm is based on the reverse-time migration algorithm in [30]. It uses the temporal Fourier transform $\hat{R}_{mn}(\omega) = \mathcal{F}_t\{R_{mn}(t)\}$ of the time traces and the Fourier transform of the transmitted pulses $\hat{T}_m(\omega) = \mathcal{F}_t\{T_m(t)\}$ to calculate the (scalar) backpropagated fields $\psi_m^{bp}(x, y, z; \omega)$ over all time traces received from each transmitter *m*, and the transmitted field $E_m^T(x, y, z; \omega)$ for each transmitter *m*. A key result from [30] is that

the RAR image $I_j^{RAR}(x,z)$ can be obtained by summing the product of these fields in the image plane $y = y_j^I$ over all transmitters and receivers, and then integrating over the angular frequency pass-band ($\omega_1 < \omega < \omega_2$) of the radar. Mathematically,

$$I_j^{RAR}(x,z) = \int_{\omega_1}^{\omega_2} \left\{ \sum_{m=1}^{N} \psi_m^{bp}(x, y_j^I, z; \omega) E_m^T(x, y_j^I, z; \omega) \right\} d\omega , \tag{4}$$

where the backpropagated field $\psi_m^{bp}(x, y_j^I, z; \omega)$ is obtained as the sum of backpropagated fields $E_{mn}^{bp}(x, y_j^I, z; \omega)$ from each receiver signal associated with pulses from transmitter m:

$$\psi_m^{bp}(x, y_j^I, z; \omega) = \sum_{n=1}^{N} E_{mn}^{bp}(x, y_j^I, z; \omega). \tag{5}$$

Since the field E_{mn}^{bp} and E_m^T are complex, the resulting RAR image is complex.

The advantage of the formulation (4)-(5) is that we can use *plane-to-plane* (P2P) backpropagation [25, 33, 29] to calculate the fields. The P2P method calculates the fields starting from an initial plane. In real-time implementations, P2P uses the fast Fourier transform (FFT) to efficiently compute the fields so that (4)-(5) can then be directly applied to RAR image reconstruction. Since the image plane can be in front of the array, we employ a full 3D (*xyz*) P2P formalism. This begins with an effective source distribution derived from the received signals $R_{mn}(\omega)$:

$$s_m^{bp}(x, y, z; \omega) = \sum_{n=1}^{N} R_{mn}^*(\omega) \delta(x - x_n) \delta(y - y_R) \delta(z - z_R) \quad , \tag{6}$$

where the coordinates of receiver *n* are (x_n, y_R, z_R), and the complex conjugate of $R_{mn}(\omega)$ is used for backpropagation. The spatial Fourier transform of $s_m^{bp}(x, y, z; \omega)$ in the *xy* plane is

$$\begin{aligned} \tilde{s}_m^{bp}(k_x, k_y, z; \omega) &= \mathcal{F}_{xy}\{ s_m^{bp}(x, y, z; \omega) \} \\ &= \frac{1}{4\pi^2} \int s_m^{bp}(x, y, z; \omega) e^{-i(k_x x + k_y y)} dx dy \\ &= \frac{1}{4\pi^2} \delta(z - z_R) e^{-ik_y y_R} \sum_{n=1}^{N} R_{mn}^*(\omega) e^{-ik_x x_n} \quad , \end{aligned} \tag{7}$$

This produces the spatial transformed field at the ground surface,

$$\tilde{\psi}_m^{bp}(k_x, k_y, z = 0; \omega) = \frac{1}{8i\pi^2 k_z} e^{-ik_y y_R} e^{ik_z z_R} \sum_{n=1}^{N} R_{mn}^*(\omega) e^{-ik_x x_n} \quad , \tag{8}$$

where $k_z = \sqrt{k^2 - k_x^2 - k_y^2}$. The ranges of k_x and k_y are restricted to the circular region where k_z is real (no evanescent fields). The field in the ground ($z < 0$) is obtained from (8) as

$$\tilde{\psi}_m^{bp}(k_x, k_y, z; \omega) = \tilde{\psi}_m^{bp}(k_x, k_y, z = 0; \omega) \cdot e^{-ik_z' z} \tag{9}$$

with $k_z' = \sqrt{n_g^2 k^2 - k_x^2 - k_y^2}$, which incorporates the refractive index of the ground material n_g. The field ψ_m^{bp} in (4) is then computed as $\psi_m^{bp}(x, y, z; \omega) = \mathcal{F}_{xy}^{-1}\{ \tilde{\psi}_m^{bp}(k_x, k_y, z; \omega) \}$, where $\mathcal{F}_{xy}^{-1}$ is the inverse spatial Fourier transform. The transmit field E_m^T in (4) is calculated in a similar way using forward propagation from the source function.

$$s_m^T(x,y,z;\omega) = \hat{T}(\omega)\delta(x-x_m)\delta(y-y_T)\delta(z-z_T) \tag{10}$$

where $T(t)$ is assumed to be an impulse ($\hat{T}(\omega)$ constant.

The RAR imaging formula (4), sums the contributions from all transmitters ($m = 1,2,\ldots,N$) at each (x,z) pixel location. However, the antenna patterns of the horns limit the sensitivity of receivers far from a given transmitter to reflections from buried objects, which effectively reduces the order of the multistatic data to less than $N = 16$ receivers per transmitter. Only receivers whose antenna patterns overlap with the antenna pattern for a given transmitter can contribute significantly to the imaging of a buried object. The other receivers contribute mostly to the background, thereby reducing object contrast against background. To correct for this, we apply windowing functions to both the receiver source function in (6), and RAR imaging formula (4). For convenience, we use rectangular unit-amplitude windowing functions. The windowed version of the source function in (6) is

$$s_m^{bp}(x,y,z;\omega) = \sum_{n=1}^{N} w^R(n-m)R_{mn}^*(\omega)\delta(x-x_n)\delta(y-y_R)\delta(z-z_R) \quad , \tag{11}$$

where $w^R(n-m)$ is unity for $|n-m| \le N_R$, and zero otherwise. The number N_R is the *multistatic degree.* For imaging, the active transmitter-receiver pairs are limited to the N_R receivers on the immediate left and right of each transmitter. The windowed version of RAR imaging formula (4) is

$$I_j^{RAR}(x,z) = \int_{\omega_1}^{\omega_2} \left\{ \sum_{m=1}^{N} w^T(x-x_m)\psi_m^{bp}(x,y_j^I,z;\omega)E_m^T(x,y_j^I,z;\omega) \right\} d\omega \quad , \tag{12}$$

where $w^T(x-x_m)$ is unity for $|x-x_m| \le N_T\Delta x$, and zero otherwise. The quantity Δx is the spacing between successive antenna pairs along the array. The *aperture weighting function* w^T limits the transmitters *m* that can contribute to the value of a pixel on column *x* of the image to those that satisfy the inequality $|x-x_m| \le N_T\Delta x$.

Each RAR image frame is reconstructed from a single frame of GPR return signals and is thus focused only in the cross-track direction. However, a buried object may appear as a bright spot in a RAR image even if the image plane does not actually contain the object. In a sequence of reconstructed RAR image frames, this bright spot will continue to rise (decrease in apparent depth) until the antenna array moves beyond the buried object. Since the apparent depth of the bright spot can be calculated from the soil refractive index, array geometry, and buried object location, we can combine the current RAR image frame with previous frames to produce *synthetic aperture radar* (SAR) image frames that are focused not only in the cross-track direction, but also in the down-track direction. The *synthetic aperture* is realized as a sequence of real apertures traced out through space along the vehicle track from the current location y_j of the vehicle backward to vehicle location $y_j - \Delta_1$ and forward to vehicle location $y_j + \Delta_2$.

SAR image frames can be reconstructed from sequences of RAR image frames using the *synthetic aperture integration formula*

$$I_j^{SAR}(x,z) = \sum_{k=j-\Delta_1}^{j+\Delta_2} I_k^{RAR}\left(x, z_{k-j}(z,n_g)\right). \tag{13}$$

Synthetic aperture integration is thus efficient, with complexity that varies linearly with the

number of pixels in an image frame. The quantity $z_{k-j}(z, n_g)$ is the apparent depth in image I_k of an object at depth z in the image plane at y_j^I. It is calculated by solving the equation

$$\text{delay}\left[(y_k, h) \text{ to } (y_j^I, z)\right] = \text{delay}\left[(y_k, h) \text{ to } (y_k^I, z_{k-j}(z, n_g))\right] \quad , \tag{14}$$

where delay (*A* to *B*) is the time delay of the radar wave in traveling from point *A* to point *B* (through air and then through soil). In practice, $\Delta_2 = 0$ and Δ_1 is computed from the extent measured from the boresight intersection with the ground plane backward to where the trailing 3 dB edge of the antenna beam intersects the ground plane. For antenna beam width θ, height h, and tilt $\phi < \theta$, we thus have $\Delta_1 = h[\tan(\phi) + \tan(\theta - \phi)]$, which evaluates to $\Delta_1 \approx 28\text{cm}$ for $(\theta, h, \phi) = (50^\circ, 30\text{ cm}, 20^\circ)$. Fig. 7 shows SAR image reconstructions (magnitudes of complex-valued pixels) with $N_T = N_R = 6$ and $n_g = 3$ for vertical down-track, vertical cross-track, and horizontal down-track slices that contain the buried object corresponding to the hyperbola shown in the signal scan of Fig. 5. The multistatic degree was selected by maximizing the ratio of spot intensity to local background level.

In the current system the complex images (I_j^{RAR} or I_j^{SAR}) are archived for later analysis while the magnitudes of the images ($|I_j^{RAR}|$ or $|I_j^{SAR}|$) are passed on to the GPR image post-processing step.

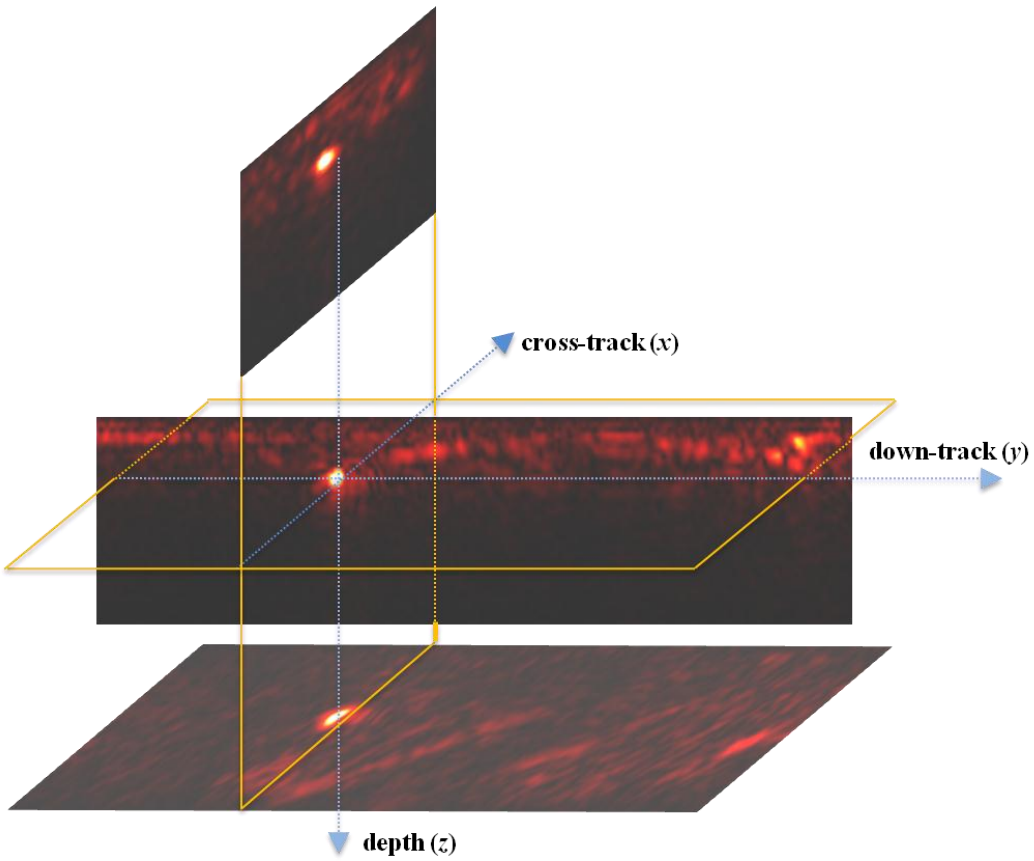

Figure 7: Multistatic SAR image reconstruction showing vertical down-track, vertical cross-track, and horizontal down-track slices that contained the buried object corresponding to the hyperbola in the signal scan of Fig. 5.

6 Foreground-Background Separation in GPR Images

GPR images reconstructed from pre-processed GPR return signals still tend to have significant residual energy at the surface and in the subsurface. GPR image post-processing suppresses residual energy not attributable to buried objects, and it is critical to the goal of separating buried objects in the foreground from soil and clutter in the background.

Fig. 8 illustrates image post-processing (foreground-background separation) on an image frame (a vertical plane image in the cross-track direction) that contains a buried metallic object. The reconstructed image frame on the top contains significant residual energy, much of which is either highly correlated or highly transient in the down-track direction. Recall that pixels in reconstructed GPR image frames are magnitudes of complex numbers, and are thus have real non-negative values. The various stages of foreground-background separation (background subtraction, image filtering, and spot restoration) are described below. The image post-processing parameters are set by default but can be over-ridden by the user, and specific steps can even be skipped altogether.

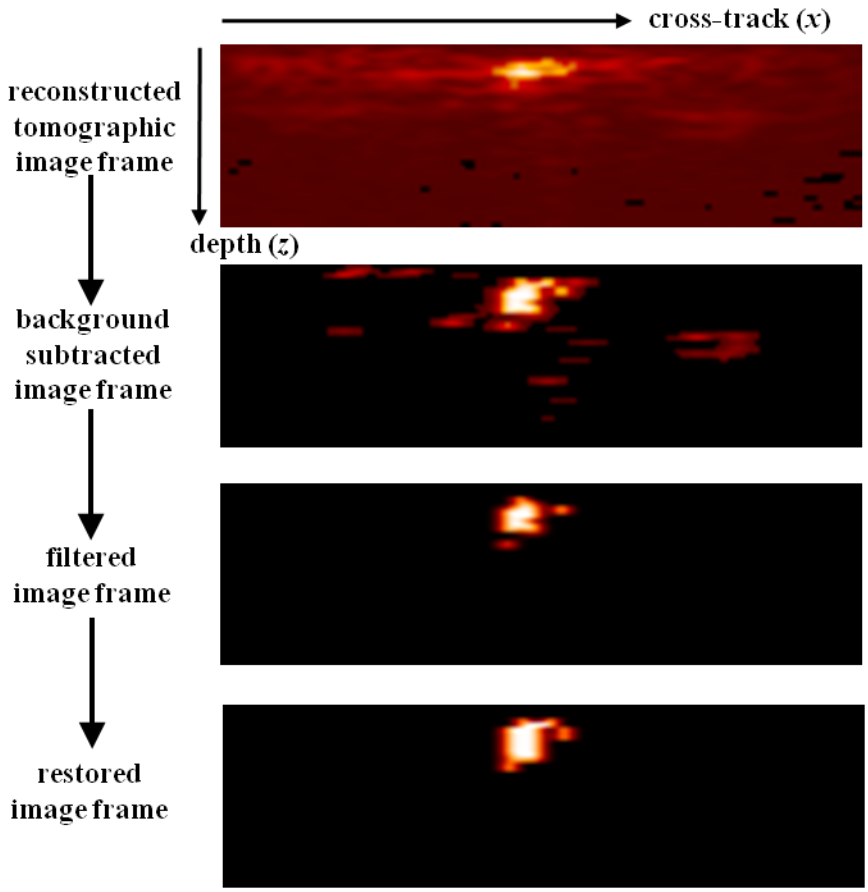

Figure 8: GPR image frames of a buried metallic object at various stages of foreground-background separation.

6.1 Background Subtraction

Our system can apply background subtraction (a) along the y (down-track) direction to individual pixels in reconstructed image frames, and then (b) along the x (cross-track) direction to individual rows in the resulting image frames, and then (c) to all pixels simultaneously in the resulting image frames. Note that most of the background energy has been removed from the background subtracted image in Fig. 8 (second from the top).

In video frame sequences, it is common practice to separate stationary background from movement in the foreground by subtracting from each pixel, the mean of corresponding pixels from previous frames [37, 48]. For GPR, this amounts to subtraction along *y*. Subtraction along *y* suppresses residual energy that is highly correlated down-track, and it makes sense when the buried objects have limited extent in *y*. Pixels in reconstructed image frames are non-negative since we pass only the magnitude of the complex images to the post-processing function. The mean of pixels (*x*,*z*) over previous reconstructed image frames $y_{k-n},\ldots,y_{k-n_0}$ is subtracted from pixel (*x*,*z*) in reconstructed image frame y_k. Large positive differences suggest an anomaly in frame y_k. Negative differences are treated as differences of zero. The

guard-band separation between image frames y_k and y_{k-n_0} should be close to the extent of a buried object, while the along-track separation between frames y_k and y_{k-n} should be perhaps an order of magnitude greater.

Background subtraction in the *x* (cross-track) direction suppresses pixels whose energies are statistically insignificant relative to other pixels in the same image frame along the same row. Subtraction along *x* makes sense when one expects the buried objects to be considerably shorter than the antenna array. $\mu(z)+n\sigma(z)$ is subtracted from each pixel on row z of the image frame, where $\mu(z)$ and $\sigma^2(z)$ are the mean and variance of nonzero pixels on row z, and $n=1$ by default. Negative differences are treated as differences of zero. Subtraction along *x* compensates for depth in the sense that larger values tend to be subtracted from rows near the surface (where return energies tend to be greater) than from deeper rows.

Next, μ_k and σ_k^2 are recursively updated as the running mean and variance over all nonzero pixels in image frames $y_0 \ldots y_k$ after background subtraction along y and then x. Pixels in frame y_k with statistically insignificant energies are suppressed by subtracting $\mu_k + n\sigma_k$ from frame y_k and treating negative differences as differences of zero ($n=1$ by default).

6.2 Image Filtering

Image filtering (a) isolates discrete buried objects in the foreground from soil and clutter in the background, and (b) suppresses residual energy that is highly transient down-track (speckle). The former goal is addressed with segmentation filters, and the latter goal is addressed with a spatially assisted median filter along y (down-track) followed by a thickness filter along z (depth). The process flow for image filtering is (i) segmentation filter 1, (ii) spatially assisted median filter along y, (iii) thickness filter along z, and (iv) segmentation filter 2. The third image from the top in Fig. 8 is filtered. In this example, the filtered output is the dominant region of highest energy (foreground *spot*) attributed to a buried metallic object. In an image frame that is free of buried objects, the filtered image will typically contain either a weak foreground spot or none at all.

The segmentation filter segments the image frame into regions of non-zero pixels using a region growing algorithm with a small prescribed search neighborhood. All pixels outside of the dominant region of highest energy (the spot) are set to zero. In this case, the segmentation filter acts as a spot filter by removing everything outside of the spot from the image. The idea of removing all but the spot is based on the simplifying assumption that for buried object detection, image frames will typically contain at most one buried object.

In sequences of GPR image frames, speckle refers to the transient spikes of energy that frequently appear and then quickly disappear as one moves through the sequence. As a spatial high pass filter, background subtraction tends to amplify the speckle inherent in radar images. Radar images are traditionally despeckled with median filters. In our case, once a segmentation filter has been applied to image frame u_k at y_k, a median filter is applied separately in the y direction to all nonzero pixels in u_{k-m} to produce filtered image frame v_{k-m}. The median filter has a short extent of $2m+1$ frames down-track. It looks both behind and ahead by m

frames, and can remove speckle that persists for as many as m frames down-track. When applied on a per-pixel basis, median filters can easily suppress too much energy. The spatially assisted y median filter (Algorithm 1) prevents this by allowing pixels to be filtered only when *all* pixels within connected groups of nearby pixels persist for less than the duration of the median filter.

Energy spots that are thin in the depth (z) direction are typically not consistent with buried objects. Spots of thickness less than a prescribed small number n_z of image rows are suppressed by applying a thickness filter along z separately to each column of the image. When applied to column x, the z filter sets $u_{k-m}(x,z)$ to zero if the number of zero pixels in the segment of column x for image rows in the range $[z-n_z, z+n_z]$ is greater than n_z. The final spot is then extracted from the z-filtered image by applying a second segmentation filter.

Algorithm 1: Spatially Assisted y Median Filter

- $\mu_{k-m}(x,z) = \text{median}\{u_j(x,z)\}_{j=k-2m}^{k}$
- $\Delta_{k-m}(x,z) = u_{k-m}(x,z) - \mu_{k-m}(x,z)$
- $\Omega_{k-m}(x,z) = \{(x',z') \in \text{neighborhood}(x,z) : u_{k-m}(x',z') > 0\}$
- $\Delta^*_{k-m}(x,z) = \min_{(x',z')\in\Omega_{k-m}(x,z)} \Delta_{k-m}(x',z')$
- $v_{k-m}(x,z) = \begin{cases} u_{k-m}(x,z) & \Delta^*_{k-m}(x,z) \le 0 \\ \mu_{k-m}(x,z) & \text{otherwise} \end{cases}$

6.3 Spot Restoration

The values of pixels in spots extracted from image frames by the second segmentation filter are typically attenuated relative to the values that they had immediately after subtraction along y. The probability of detecting buried objects can be improved by using the spot restoration algorithm (Algorithm 2) (a) to expand the spot with additional pixels as appropriate, and (b) to restore attenuated spot pixel values to the un-attenuated values that they had after subtraction along y. The last image in Fig. 8 contains a restored spot. Notice that the restored spot is larger and brighter than the filtered spot.

If u_k is the image after subtraction along y that corresponds to filtered image v_k, the restored spot is grown in u_k from locations of pixels in the filtered spot (spot(v_k)). For region growing, the seed pixel is the first pixel in spot(v_k) and the search neighborhood is typically the same as for the segmentation filter. The region growing threshold u^* is computed as a prescribed percentile ($\rho = 25\%$ by default) of u_k values at locations of pixels

in spot(v_k). Details are provided in Algorithm 2.

Algorithm 2: Spot Restoration

1. Compute segmentation threshold for spot expansion:
   - $u^* = \underset{(x,z)\in spot(v_k)}{\text{percentile}}\ \rho \quad u_k(x,z)$
2. Expand the spot:
   - $v_k \leftarrow u_k$
     $v_k(x,z) = 1 + u^* \quad \forall (x,z) \in spot(v_k)$
   - (x_{seed}, z_{seed}) = first element of $\text{spot}(v_k)$
     $\text{spot}(v_k) = \text{regionGrow}(v_k, (x_{seed}, z_{seed}), u^*, \text{neighborhood})$
3. Restore the spot pixels:
   - $v_k(x,z) = \begin{cases} u_k(x,z) & (x,z) \in \text{spot}(v_k) \\ 0 & \text{otherwise} \end{cases}$

7 The Weighted Spot Ratio Detection Statistic

In some GPR applications, the final output product is a 3D image of the subsurface that is inspected off-line for buried objects by a human operator. Other GPR applications (such as demining) require buried object detection in real-time. In real-time image-based detection, a buried object detection statistic must be computed in real-time for each GPR image frame. In this section, we propose an energy-based statistic for buried object detection in GPR image frames that is relatively insensitive to roughness in the road.

When searching for buried objects, it is common practice to apply classifiers to small portions of GPR data that have been pre-screened by detectors [45]. These detectors typically require no training. They use efficient algorithms to search for anomalies in GPR data that are consistent with objects. The classifiers however, must normally be trained. More complex algorithms are used to discriminate specific objects either from false positives or from other objects by type.

Buried objects can be found by analyzing either GPR return signals (as in most of the literature) or tomography images reconstructed from GPR return signals. Classifiers for GPR return signals have been studied extensively [50, 38, 3, 4, 21, 28, 51, 43, 22, 52, 53, 42, 36, 19, 20, 18, 47, 40]. Neural network classifiers have been applied to scattering parameter features [50, 38, 3], bispectrum features [4], and geometry features of principal component depth planes, where objective functions for mean-squared error and area under the ROC curve are used [21, 28]. Support and relevance vector machines (SVMs and RVMs) have been applied directly to the return signal [51] and to texture features derived from 3D arrays of return signal samples [43]. Hidden Markov Models (HMMs) based on edges in scans (sequences of return

signals along the track) have been constructed for hyperbola matching [22, 52], as hyperbolic arcs in scan data are characteristic of buried objects. Hyperbolas have also been matched by applying polynomial fits [53], Hough transforms (for both hyperbolas and piecewise linear approximations) [42], and genetic algorithms [36] to sequences of return signals along the track. Fuzzy K-means classifiers have been applied to feature vectors based on principal components (PCs) of return signals [19], edge strength features derived from sequences of return signals along the track [20], and edge histogram descriptors or EHDs (motivated by MPEG-7) that capture distributions of edge orientation in both xy and yz planes [18]. Matched filters have been applied to spectra of individual return signals [47]. Singular values and singular vectors of the Wigner time-frequency transform of individual return signals were proposed as feature vectors in [40].

Classifiers for GPR tomography images have been studied far less extensively. One approach uses time frequency transforms for columns of GPR tomography images that cut through suspected objects for classification [23].

Detectors, on the other hand, are typically energy-based [45, 44, 10, 41], and are usually applied to GPR return signals only after background has been removed. We propose a detection statistic for GPR image frames that is also energy-based. Perhaps the most obvious detection statistic is the *spot energy* $e_k \geq 0$ of the restored spot in the image frame at y_k. Recall that values of pixels in the restored spot are drawn from the image frame at y_k immediately after background subtraction in the y direction. Fig. 9 shows various time series of detection statistic values (or time series for short) generated from a sequence of multistatic SAR image frames reconstructed along a 297 meter rough off-road track in a desert region of the southwest United States. The antenna array was mounted 30 cm above ground level at a forward tilt of 20° from vertical, and the vehicle was moving at 8 km/hr. The diamond markers show locations of buried emplacements (both metallic and non-metallic). Fig. 9(a) shows the spot energy time series $\{e_k\}$ generated from a sequence of reconstructed image frames that were not post-processed. Fig. 9(b) shows $\{e_k\}$ generated from the corresponding sequence of post-processed image frames. The time series $\{e_k\}$ is highly nonstationary (it has local trends). In particular, as the track becomes more rough, the likelihood of anomalous backscatter from the surface increases, along with e_k. So as the track becomes more rough, the time series $\{e_k\}$ trends upward and the rate of false positives tends to increase. In Fig. 9(a-b), one can see that the ratio of spot energy at emplacement locations to spot energy elsewhere is much greater when the images are post-processed. It is clear from these two time series that foreground-background separation is essential for energy-based buried object detection in GPR tomography images. Nevertheless, even when generated from post-processed image frames, $\{e_k\}$ can still be highly nonstationary.

In classical time series analysis, a nonstationary time series is often detrended by subtracting a moving average from each time series sample. However, in many applications detection of buried objects is inherently causal, *i.e.* each buried object must be detected *before* the vehicle passes over it. This means that for our problem, the moving window must trail the current location of the vehicle down-track and the moving window that applies to a specific

detection time series sample must trail that sample. Unfortunately, trailing window moving averages react slowly to sudden changes in track conditions (such as surface roughness, soil type, moisture content, *etc.*), and this can lead to false positives in the detrended time series near locations of sudden change.

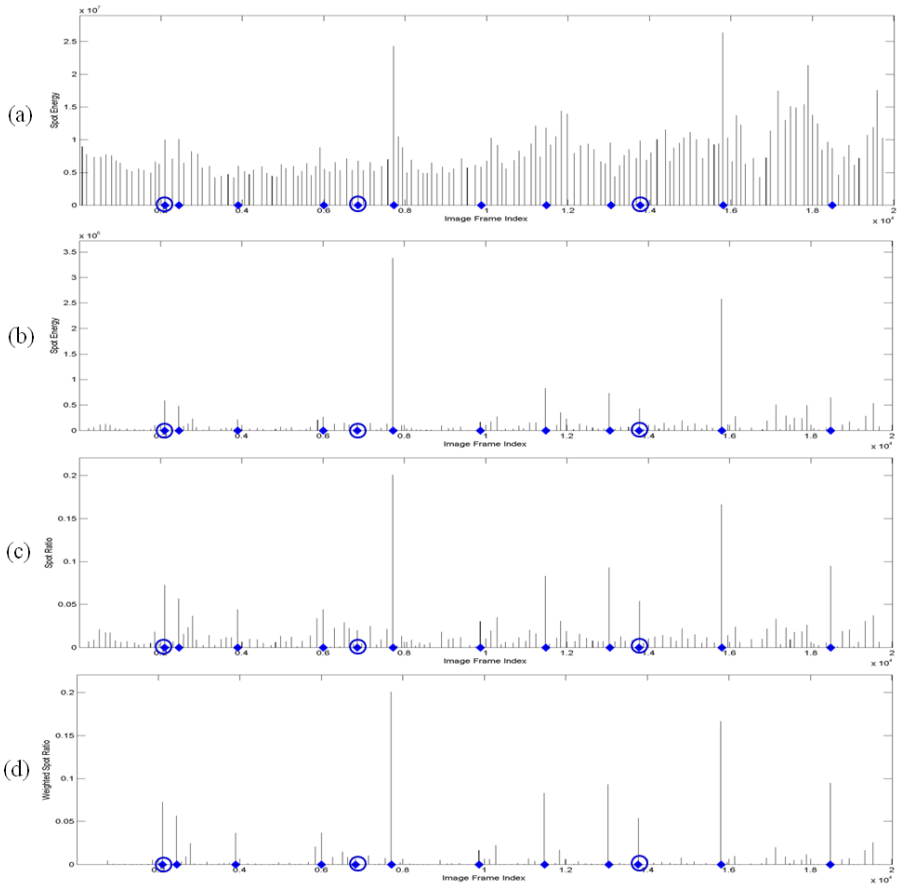

Figure 9: Detection time series of (a) spot energy without image post-processing, and (b-d) spot energy, spot ratio, and weighted spot ratio with image post-processing along a 297 m rough off-road track. Buried objects are annotated with diamond markers. The diamond markers are circled for buried objects that are non-metallic .

Rather than attempting to detrend a time series based on a detection statistic that is inherently nonstationary, we propose a more stationary detection statistic. Spot energy can be mostly detrended by dividing the energy inside the spot (the spot energy e_k) by a stable estimate of the level of energy outside the spot (the level of frame clutter c_k) to form the finite non-negative *spot ratio*

$$r_k \triangleq \begin{cases} e_k / c_k & c_k > 0 \\ 0 & c_k = 0 \end{cases} \tag{15}$$

In (15), c_k is computed as the median of pixels in *reconstructed* image frame k. The time series $\{c_k\}$ will be highly correlated with the time series in Fig. 9(a) because the spot extracted

from a reconstructed image (such as the top image in Fig. 8) will typically contain most of the frame pixels, and frame medians tend to be highly correlated with frame energies. As illustrated in Fig. 9(c), the spot ratio detection series $\{r_k\}$ is quite stationary and mostly free of local trends associated with changes in track conditions such as roughness in the surface.

Noise in $\{r_k\}$ can be a nuisance to operators of the system. If the operator chooses to monitor $\{r_k\}$ in real time as the vehicle proceeds down-track, noise in the time series makes it more difficult to mentally distinguish detections from background anomalies. If the operator instead chooses to monitor the associated sequence of post-processed tomography image frames in real-time, the amount of visible image clutter increases with noise in $\{r_k\}$, making it more difficult to mentally distinguish detections from background anomalies in the images. Noise in $\{r_k\}$ can be suppressed by computing the product of r_k and the *spot ratio weighting function* $w(r_k)$ to produce the *weighted spot ratio*

$$\tilde{r}_k \triangleq w(r_k) r_k \tag{16}$$

We propose a piecewise linear weighting function of the form

$$w(r_k) = \begin{cases} w_L & r_k \le R_L \\ \dfrac{w_H - w_L}{R_H - R_L}(r_k - R_L) + w_L & R_L < r_k < R_H \\ w_H & r_k \ge R_H \end{cases} \tag{17}$$

for $0 \le w_L \le w_H$ and $0 \le R_L < R_H$. $w(r_k)$ becomes a penalty function when $0 \le w_L < w_H \le 1$. We suppress noise in $\{r_k\}$ by using the weighting function parameters

$$\begin{aligned} (w_L, w_H) &= (0.01, 1), \\ (R_L, R_H) &= (n_L \mu_r, n_H \mu_r), \\ (n_L, n_H) &= (1, 10) \end{aligned} \tag{18}$$

where μ_r is computed as the median of spot ratio values over the first $K = 100$ image frames for which $r_k > 0$.

Fig. 9(d) shows the weighted spot ratio time series $\{\tilde{r}_k\}$ that corresponds to the spot ratio time series $\{r_k\}$ in Fig. 9(c). One would not expect the detection-false alarm rate performance of $\tilde{r}_k$ to be much different than for r_k because $\tilde{r}_k$ is a monotonically non-decreasing function of r_k. However, visualization displays based on $\{\tilde{r}_k\}$ are less noisy and potentially more useful to system operators.

8 System Performance Characterization

The performance of a GPR-based system for detecting buried objects is normally characterized with ROC curves. For GPR, it is customary to plot detection probability vs. the number of false positives per square meter. The number of false positives per square meter is estimated as the number of false positives divided by the product of vehicle travel distance down-track and the cross-track extent of the antenna array. Detection probability is estimated as the number of emplacements that were detected divided by the number that should have

been detected. An emplacement should have been detected only if the antenna array was driven over it. An emplacement is thus counted only if its distance to the vehicle track is less than half the cross-track extent of the antenna array.

ROC curve estimates require a vehicle track along a sequence of emplacements. The vehicle track is the GPS location of the antenna array midpoint proceeding down-track. Emplacement locations are surveyed prior to performance evaluation. The location of a buried object in a reconstructed image frame is estimated from the pixel location of the spot centroid, the GPS locations of the antenna array endpoints for that frame, and frame geometry. Frame geometry includes pixel width and height, height above ground level for the first row of pixels, and distance from the array start point to the first column of pixels.

ROC curve estimates also require a series of detection statistic values. Detections within a prescribed tolerance Δ of emplacement locations are considered valid. False positives are disallowed within $\pm\Delta$ meters down-track of detections or other false positives. A ROC curve is thus most easily estimated from a time series that has first been peak filtered so as to ensure a down-track separation of at least Δ between nonzero peaks. Δ accounts for (1) uncertainty in GPS estimates of vehicle location down-track relative to surveyed locations of emplacements, and (2) uncertainty in object locations introduced by radars that sense objects over extended intervals of vehicle location down-track.

Strengths of emplacements relative to background provide a second very different measure of system performance. Unlike ROC curves, relative strengths are estimated from unfiltered time series. The relative strength of an emplacement is the value of its detection statistic divided by the background level. The background level is the mean of detection statistic values over all nonzero series samples that are separated down-track from every emplacement by more than Δ. The relative strength overall is the mean over all emplacements of relative strengths.

8.1 Spot Energy vs. Weighted Spot Ratio

Fig.10(a) shows ROC curves for the rough off-road track of Fig.9 with $\Delta = 0.5\mathrm{m}$. The ROC curve for $\{e_k\}$ improves when the image frames are first post-processed. The ROC curve for $\{\tilde{r}_k\}$ is better than for $\{e_k\}$ because nonstationarity due to roughness in the track has been mostly removed. Using $\{\tilde{r}_k\}$, a detection probability of $10/12 > 0.83$ was achieved with no false positives. The emplacement corresponding to diamond marker five was not detected. It is important to realize that although the false positives that compete with the weaker detection at diamond marker seven were not emplaced for this exercise, some may correspond to pre-existing buried objects.

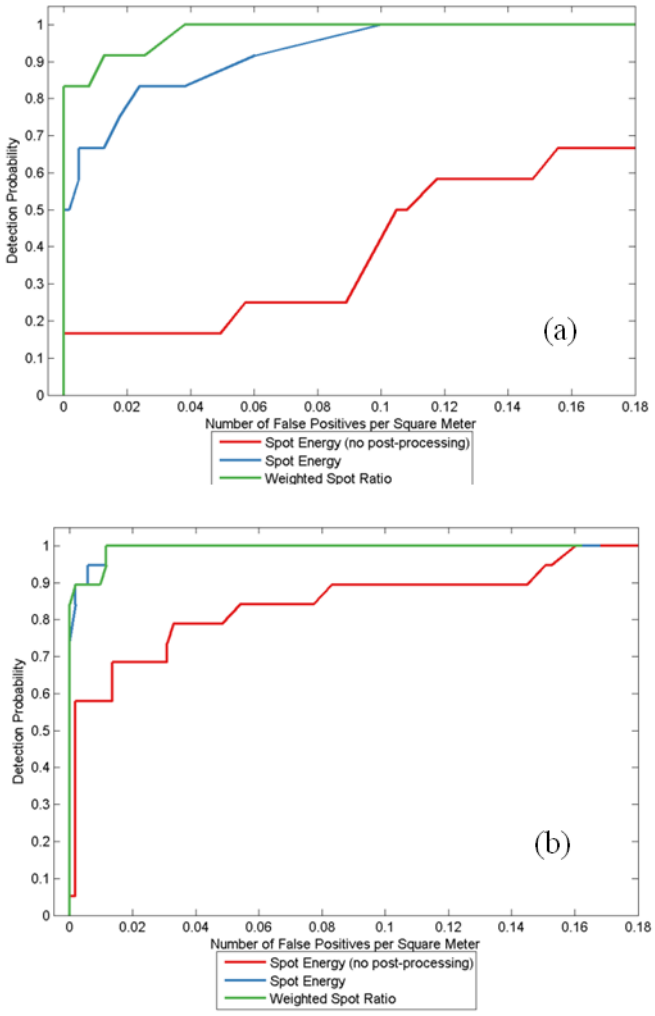

Figure 10: ROC curves for detection time series of spot energy without image post-processing, spot energy with image post-processing and weighted spot ratio with image post-processing along (a) the 297 m rough off-road track from Fig. 9, and (b) a 244 m track over flat rocky soil.

Fig.10(b) shows ROC curves for a 244 m track over flat rocky soil in the vicinity of the previous rough track (Fig. 9) with $\Delta = 1.5\text{m}$ (as uncertainty in emplacement locations was greater on this run). These ROC curves were based on locations of emplacements and previously buried objects (both metallic and non-metallic). The antenna array was mounted 30 cm above ground level at a forward tilt of 20° from vertical, and the vehicle was moving at 8km/hr. Once again, the ROC curve for $\{e_k\}$ improves when the image frames are first post-processed. However this time, it improves less because e_k is corrupted less by roughness in the track. Also, when the images are first post-processed, the ROC curve for $\tilde{r}_k$ is now comparable to the ROC curve for $\{e_k\}$ because $\{e_k\}$ is fairly stationary to begin with. A detection probability of $16/19 > 0.84$ was achieved with no false positives using $\{\tilde{r}_k\}$, and a

detection probability of $17/19 > 0.89$ was achieved with one false positive.

8.2 Monostatic vs. Multistatic Imaging through Real vs. Synthetic Apertures

We now provide an example in which system performance is characterized as a function of how the tomography images were reconstructed. Images of the subsurface along a 293m rough off-road track near the previous tracks were generated in both monostatic and multistatic mode through real and synthetic apertures to produce both real-aperture radar (RAR) and synthetic aperture radar (SAR) images. This time, the antenna array was mounted 30 cm above ground level at a forward tilt of 30° from vertical, and the vehicle was moving at 8 km/hr. The multistatic degree was ± 6 receivers for each transmitter and the aperture weighting function for coherent imaging was nonzero over ± 6 adjacent transmitters. For this run, the down-track extent of the synthetic aperture was computed to extend approximately 28 cm backward from the intersection of the boresight axis of the radar with the ground plane.

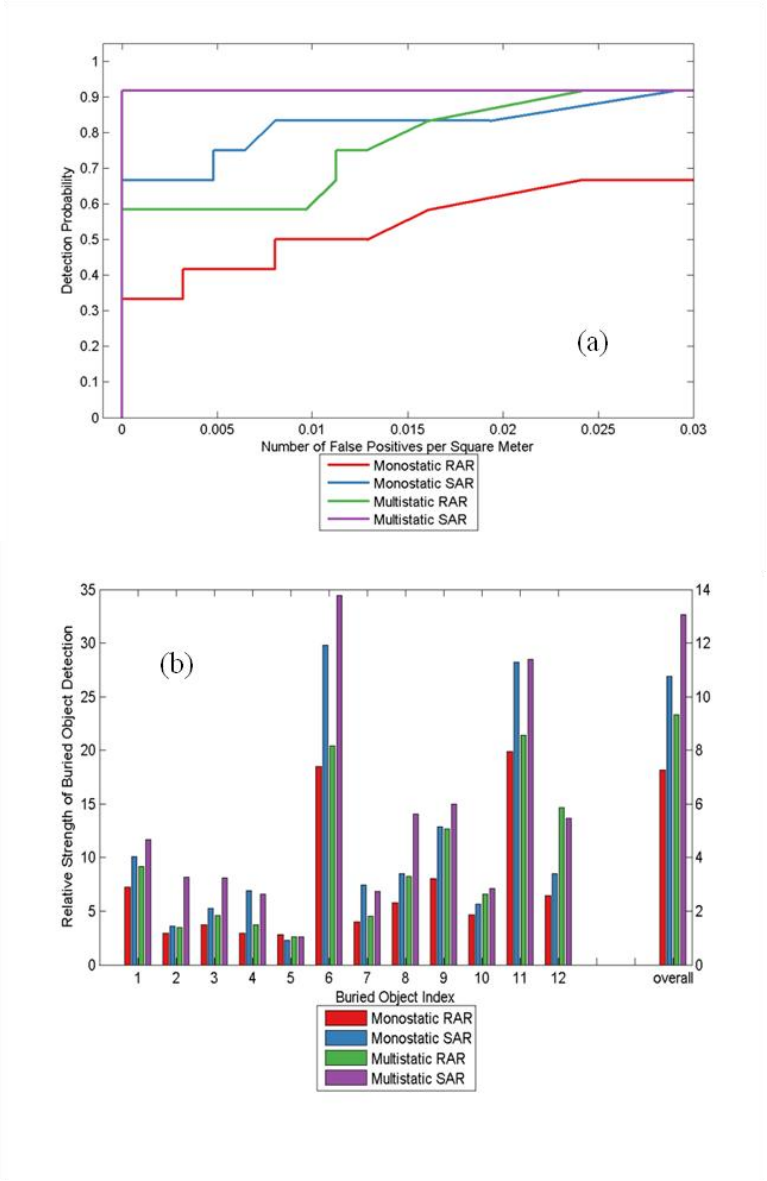

Figure 11: (a) ROC curves, and (b) bar charts of buried object relative detection strengths for detection time series of weighted spot ratios derived from sequences of monostatic and multistatic RAR and SAR image frames along a 297 m rough off-road track.

Fig.11(a) shows ROC curves for $\{\tilde{r}_k\}$ with $\Delta = 0.5$ m. Synthetic aperture imaging led to improved performance in both monostatic and multistatic modes. Multistatic mode led to improved performance in subsurface imaging through both real and synthetic apertures. The best overall performance was achieved by multistatic imaging through a synthetic aperture. In that case, a detection probability of $11/12 > 0.91$ was achieved with no false positives. The remaining object was not detected.

Fig.11(b) shows bar charts based on $\{\tilde{r}_k\}$ for relative strengths of buried object detections based on spot ratio. Overall and for most individual buried objects (a) monostatic SAR was stronger than monostatic RAR, (b) multistatic SAR was stronger than multistatic RAR,

(c) multistatic RAR was stronger than monostatic RAR, and (d) multistatic SAR was stronger than monostatic SAR. The best overall performance was again achieved by multistatic imaging through a synthetic aperture.

9 Summary

We have presented an overview of our real-time multistatic underground imaging radar (MUIR) system and shown its performance over tracks with buried emplacements. The system consists of $N = 16$ transmitter/receiver pairs that collect $N^2 = 256$ time signals in each data frame, as opposed to only $N = 16$ time signals in each frame for typical monostatic GPR array systems. A sophisticated real-time processing system based on reverse-time migration combined with plane-to-plane backpropagation reduces the data frame to an image of the subsurface in a vertical plane in front of the tilted array. A robust method for separating bright spots associated with buried objects from background variation is applied to the image and a weighted spot energy ratio statistic is calculated to detect the presence of buried objects. These methods exploit the additional information obtained from measuring the bistatic scattering, significantly enhancing the visualization and detection of buried objects in tests conducted in the desert Southwest compared to a monostatic system. Measurements of the ratio of image spot amplitude to background for typical buried objects imply useful information is collected by over half of the receivers for each transmitter. To the authors' knowledge, this system is the first real-time *multistatic* GPR imaging system capable of field operation.

The overall conclusion is that multistatic GPR arrays are now a practical reality and show good object detection performance in field tests. However, we are only beginning to exploit the information potential of multistatic GPR data. The multiple bistatic measurements would be particularly useful in classifying buried objects, enabling better estimates of their scattering properties. The multistatic data also enables time-reversal techniques to be used to enhance object visibility and detection. We expect to see dramatic improvements in detection and classification performance as more sophisticated algorithms specifically designed for multistatic GPR data are developed and incorporated into our real-time processing system.

10 Acknowledgements

The authors wish to acknowledge Steven Bond as lead for data acquisition, Phillip Top for his work with the vehicle-based GPS systems, and both for their many contributions to vehicle on-board signal handling and storage. The authors also wish to acknowledge the extraordinary effort by the LLNL UWB radar team in the design, construction, and deployment of the LLNL GPR system.

This work performed under the auspices of the U.S. Department of Energy by Lawrence Livermore National Laboratory under Contract DE-AC52-07NA27344.

References

[1] I. Aliferis and T. Savelyev and M. J. Yedlin and J-Y. Dauvigne and A. Yarovoy and C. Pichot and L. Ligthart. Comparison of the diffraction stack and time-reversal imaging

algorithms applied to short-range UWB scattering data. *IEEE Int. Conf. Ultra-Wideband*, pages 618-621, 2007. IEEE.

[2] H. Ammari and E. Iakovleva and D. Lesselier. A MUSIC algorithm for locating small inclusions buried in a half-space from the scattering amplitude at a fixed frequency. *Multiscale Modeling and Simulation*, 3(3):579-628, 2005.

[3] M. Azimi-Sadjadi and D. Poole and S. Seedvash and K. Sherbondy and S. Stricker. Detection and Classification of Dielectric Anomalies using a Separated Aperture Sensor and a Neural Network Discriminator. *IEEE Trans. Instrum. Meas.*, 41(1):137-143, 1992.

[4] A. Balan and M. Azimi-Sadjadi. Detection and Classification of Buried Dielectric Anomalies by Means of the Bispectrum Method and Neural Networks. *IEEE Trans. Instrum. Meas.*, 44(6):998–1002, 1995.

[5] L. Bellomo and S. Pioch and others. Time reversal experiments in the microwave range: description of the radar and results. *Prog. Electromag. Res.*, 104:427-448, 2010.

[6] H. Brunzell. Detection of shallowly buried objects using impulse radar. *IEEE Trans. Geos. Rem. Sens.*, 37:875-886, 1999.

[7] D. Carevic. Clutter reduction and target detection in ground penetrating radar data using wavelets. *Detection and Remediation Technologies for Mines and Minelike Targets IV*, pages 973-978, 1999. SPIE.

[8] D. Carevic. Kalman filter-based approach to target detection and target-background separation in ground-penetrating radar data. *Detection and Remediation Technologies for Mines and Minelike Targets IV*, pages 1284-1288, 1999. SPIE.

[9] V. Chatelee and A. Dubois and others. Real data microwave imaging and time reversal. *IEEE APS Int. Symp.*, pages 1793-1796, 2007. IEEE.

[10] L. Collins and P. Torrione and V. Munshi and C. Throckmorton and Q. Zhu and J. Clodfelter and S. Frasier. Algorithms for Land Mine Detection using the NIITEK Ground Penetrating Radar. *Proc. SPIE Int. Soc. Opt.*, pages 709–718, 2002. SPIE.

[11] T. Counts and A. Gurbuz and others. Multistatic ground-penetrating radar experiments. *IEEE Trans. Geos. Rem. Sens.*, 45(8):2544-2553, 2007.

[12] A. Cresp and I. Aliferis and M. J. Yedlin and C. Pichot and J.-Y. Dauvignac. Investigation of time-reversal processing for surface-penetrating radar detection in a multiple-target configuration. *Proc. 5th European Radar Conference*, pages 144-147, 2008.

[13] A. Cresp and M. J. Yedlin and others. Comparison of the time-reversal and

SEABED imaging algorithms applied on ultra-wideband experimental SAR data. *Proc. 7th European Radar Conference*, pages 360-363, 2010.

[14] D. Daniels. A review of GPR for landmine detection. *Int. J. Sens. Imag.*, 7(3):90-123, 2006.

[15] D. Daniels. An assessment of the fundamental performance of GPR against buried landmines. *Detection and Remediation Technologies for Mines and Minelike Targets XII*, pages 65530G-1--65530G-15, 2007. SPIE.

[16] M. Fink and D. Cassereau and others. Time-reversed acoustics. *Rep. Prog. Phys.*, 63:1933-1995, 2000.

[17] M. Fink and C. Prada. Acoustic time-reversal mirrors. *Inverse Problems*, 17:R1-R38, 2001.

[18] H. Frigui and P. Gader. Detection and discrimination of land mines in ground-penetrating radar based on edge histogram descriptors and a possibilistic K-Nearest neighbor classifier. *IEEE Trans. Fuzzy Sys.*, 17(1):185-199, 2009.

[19] H. Frigui and P. Gader and K. Satyanarayana. Landmine Detection with Ground Penetrating Radar using Fuzzy k-Nearest Neighbors. *Proc. IEEE Int. Conf. Fuzzy Sys.*, pages 1745–1749, 2004. IEEE.

[20] P. Gader and J. Keller and H. Frigui and H. Liu and D. Wang. Landmine Detection using Fuzzy Sets with GPR Images. *Proc. IEEE Int. Conf. Fuzzy Sys., Vol. 1*, pages 232–236, 1998. IEEE.

[21] P. Gader and W. Lee and J. Wilson. Detecting Landmines with Ground-Penetrating Radar using Feature-Based Rules, Order Statistics, and Adaptive Whitening. *IEEE Trans. Geosci. Remote Sens.*, 42(11):2522–2534, 2004.

[22] P. Gader and M. Mystkowski and Y. Zhao. Landmine Detection with Ground Penetrating Radar using Hidden Markov Models. *IEEE Trans. Geosci. Remote Sens.*, 39(6):1231–1244, 2001.

[23] G. Gaunaurd and L. Nguyen. Detection of Land-mines using Ultra-Wideband Radar Data and Time-Frequency Signal Analysis. *IEE Proc.-Radar Sonar Navig.*, 151(5):307-316, 2004.

[24] C. Gilmore and I. Jeffrey and J. LoVetri. Derivation and comparison of SAR and frequency-wavenumber migration within a common inverse scalar wave problem formulation. *IEEE Trans. Geos. Rem. Sens.*, 44(6):1454-1461, 2006.

[25] Joseph W. Goodman. *Introduction to Fourier Optics*. McGraw-Hill, New York, NY, 1996.

[26] L. Jofre and A. Broquetas. UWB tomographic radar imaging of penetrable and impenetrable objects,. *Proc. IEEE*, 97(2):451-464, 2009.

[27] J. Kositsky and P. Milanfar. A forward-looking high-resolution GPR mine detection system. *Proc. SPIE Conf. on Detection and Remediation Technologies for Mines and Minelike Targets IV*, pages 1052–1062, 1999. SPIE.

[28] W-H. Lee and P. Gader and J. Wilson. Optimizing the Area Under a Receiver Operating Characteristic Curve With Application to Landmine Detection. *IEEE Trans. Geosci. Remote Sens.*, 45(2):389-397, 2007.

[29] Sean Kenneth Lehman. *Superresolution of Buried Objects in Layered Media by Near-Field Electromagnetic Imaging*. PhD thesis, University of California at Davis, Davis, CA, 2000.

[30] C. J. Leuschen and R. G. Plumb. A Matched-Filter-Based Reverse-Time Migration Algorithm for Ground-Penetrating Radar Data. *IEEE Trans. Geosci. Remote Sens.*, 39(5):929-936, 2001.

[31] D. Lloyd and I. D. Longstaff. Ultra-wideband multi-static SAR for the detection and location of landmines. *Proc. 4th European Conference on Synthetic Aperture Radar*, 2002.

[32] D. Lloyd and I. D. Longstaff. Ultra-wideband multistatic SAR for the detection and location of landmines. *IEE Proc. Radar Sonar Navigation*, 150(3):158-164, 2003.

[33] Jeffrey Edward Mast. *Microwave Pulse-echo Radar Imaging for the Nondestructive Evaluation of Civil Structures*. PhD thesis, University of Illinois at Urbana-Champaign, Urbana, IL, 1993.

[34] G. Micolau and M. Saillard. DORT method as applied to electromagnetic subsurface imaging. *Radio Sci.*, 38(3):4-1--4-12, 2003.

[35] G. Micolau and M. Saillard and P. Borderies. DORT method as applied to ultrawideband signals for detection of buried objects. *IEEE Trans. Geos. Rem. Sens.*, 41(8):1813-1820, 2003.

[36] E. Pasolli and F. Melgani and M. Donelli. Automatic Analysis of GPR Images: A Pattern Recognition Approach. *IEEE Trans. Geosci. Remote Sens.*, 47(7):2206-2217, 2009.

[37] M. Piccardi. Background subtraction techniques: a review. *IEEE Int. Conf. Sys. Man, Cybernetics*, pages 3099-3104, 2004. IEEE.

[38] G. Plett and T. Doi and D. Torrieri. Mine Detection using Scattering Parameters and an Artificial Neural Network. *IEEE Trans. Neural Networks*, 8(6):1456–1467, 1997.

[39] M Saillard and P. Vincent and G. Micolau. Reconstruction of buried objects surrounded by small inhomogeneities. *Inverse Problems*, 16:1195-1208, 2000.

[40] T. Savelyev and L. van Kempen and H. Sahli and J. Sachs and M. Sato. Investigation of Time-Frequency Features for GPR Landmine Discrimination. *IEEE Trans. Geosci. Remote Sens.*, 45(1):118-129, 2007.

[41] L. Tang and P. Torrione and C. Eldeniz and L. Collins. Ground Bounce Tracking for Landmine Detection using a Sequential Monte Carlo Method. In R. Harmon and J. T. Broach and J. Holloway Jr., editors, *Detection and Remediation Technologies for Mines and Minelike Targets XII*, pages 728–735, 2007. SPIE.

[42] S. L. Tantum and Y.Wei and V. S. Munshi and L. M. Collins. A Comparison of Algorithms for Landmine Detection and Discrimination using Ground Penetrating Radar. *Proc. SPIE Conf. on Detection and Remediation Technologies for Mines and Minelike Targets VII*, pages 728–735, 2002. SPIE.

[43] P. Torrione and L. Collins. Application of Texture Feature Classification Methods to Landmine/Clutter Discrimination in Off-road GPR Data. *Proc. IGARSS*, pages 1621–1624, 2004.

[44] P. Torrione and L. Collins and F. Clodfelter and S. Frasier and I. Starnes. Application of the LMS Algorithm to Anomaly Detection using the Wichmann/NIITEK Ground Penetrating Radar. In Russel S. Harmon and John H. Holloway Jr. and J. T. Broach, editors, *Proc. SPIE Detection and Remediation Technologies for Mines and Minelike Targets VIII*, pages 1127-1136, 2003. SPIE.

[45] P. Torrione and C. Throckmorton and L. Collins. Performance of an adaptive feature-based processor for a wideband ground penetrating radar system. *IEEE Trans. Aerospace and Electronic Sys.*, 42(2):644-658, 2006.

[46] H. Tortel and G. Micolau and M. Saillard. Decomposition of the time reversal operator for electromagnetic scattering. *J. Electromagnetic Waves App.*, 13:687-719, 1999.

[47] J. Wilson and P. Gader and W-H. Lee and H. Frigui and K. Ho. A Large-Scale Systematic Evaluation of Algorithms using Ground-Penetrating Radar for Landmine Detection and Discrimination. *IEEE Trans. Geosci. Remote Sens.*, 45(8):2560-2572, 2007.

[48] C. Wren and A. Azarhayejani and T. Darrell and A. Pentland. Pfinder: Real-time tracking of the human body. *IEEE Trans. Pattern Anal. and Machine Intell.*, 19(7):780-785,

1997.

[49] R. Wu and A. Clement and J. Li and E. Larsson and M. Bradley and K. Habersat and G. Maksymonko. Adaptive ground bounce removal. *Electronics Letters*, 37:1250–1252, 2001.

[50] C. Yang. Landmine Detection and Classification with Complex-Valued Hybrid Neural Network using Scattering Parameters Dataset. *IEEE Trans. Neural Networks*, 16(3):743–753, 2005.

[51] J. Zhang and Q. Liu and B. Nath. Landmine Feature Extraction and Classification of GPR Data Based on SVM Method. *Proc. Int. Symp. Neural Networks, Part I*, pages 636–641, 2004.

[52] Y. Zhao and P. Gader and P. Chen and Y. Zhang. Training DHMMs of Mine and Clutter to Minimize Landmine Detection Errors. *IEEE Trans. Geosci. Remote Sens.*, 41(5):1016–1024, 2005.

[53] Q. Zhu and L. Collins. Application of Feature Extraction Methods for Landmine Detection using the Wichmann/Niitek Ground-Penetrating Radar. *IEEE Trans. Geosci. Remote Sens.*, 43:81-85, 2005.

[54] X. Zhuge and T. G. Savelyev and others. UWB array-based radar imaging using modified Kirchhoff migration. *IEEE Conf. Ultra-Wideband*, pages 175-178, 2008. IEEE.